metals

MDPI

Article

Mechanosynthesis of Nanocrystalline Biphasic Ni-Fe Alloy Powders by Mechanical Alloying and Their Structural and Thermal Characterization

Myriam Azabou [1], Wael Ben Mbarek [2], Asma Wederni [2], Sumaya Almenia [3], Mohamed Khitouni [3] and Joan-Josep Suñol [2,*]

[1] Laboratory of Inorganic Chemistry, LR17-ES-07, Faculty of Science, University of Sfax, P.O. Box 1171, Sfax 3018, Tunisia; mymyriamazabou@gmail.com
[2] Department of Physics, Campus Montilivi, University of Girona, 17073 Girona, Spain; u1930157@campus.udg.edu (W.B.M.); asma.wederni@udg.edu (A.W.)
[3] Department of Chemistry, College of Science, Qassim University, Buraydah 51452, Saudi Arabia; 3582@qu.edu.sa (S.A.); kh.mohamed@qu.edu.sa (M.K.)
* Correspondence: joanjosep.sunyol@udg.edu

Abstract: An equiatomic Ni-Fe alloy was synthesized through mechanosynthesis, under an argon atmosphere using a planetary ball mill, after 100 h. To assess the phase stability, the alloy was subsequently annealed at 923.15 K for 2 h. At the end of mechanosynthesis, X-ray diffraction analysis revealed the formation of two distinct solid phases, FCC γ-NiFe (wt% = 90.3%) and BCC α-FeNi (wt% = 9.7%). The lattice parameter of the FCC phase stabilized at 3.5748 Å, whereas the BCC phase exhibited a lattice parameter of 2.6608 Å. The average crystallite size was determined to be around 7 nm with the lattice strains quantified as 0.48% for both phases. This significant refinement of microstructure indicates extensive plastic deformation within the grains. Scanning electron microscopy revealed an angular particle morphology with an average particle size of 8.15 μm. Differential scanning calorimetry (DSC) analysis identified an exothermic transition at 623.15 K, corresponding to the Curie temperature of nickel, and another one at 873.15 K, attributed to the Curie temperature of Ni_3Fe. These results demonstrate the efficiency of mechanosynthesis in producing biphasic Ni-Fe nanomaterials with tailored properties, characterized by a dominant FCC phase with a highly deformed nanocrystalline structure. These findings highlight the great influence of mechanical milling on the structural properties of the Ni-Fe alloy in terms of a high density of stored crystalline defects.

Keywords: Ni-Fe alloy; nanostructure; mechanosynthesis; X-ray diffraction; thermal; defects; annealing

Received: 21 January 2025
Revised: 21 February 2025
Accepted: 26 February 2025
Published: 28 February 2025

Citation: Azabou, M.; Ben Mbarek, W.; Wederni, A.; Almenia, S.; Khitouni, M.; Suñol, J.-J. Mechanosynthesis of Nanocrystalline Biphasic Ni-Fe Alloy Powders by Mechanical Alloying and Their Structural and Thermal Characterization. *Metals* **2025**, *15*, 270. https://doi.org/10.3390/met15030270

1. Introduction

Nanostructured Ni-Fe alloys, developed through mechanical milling, are a significant focus of research in the field of advanced materials due to their unique microstructural and physical properties [1]. Additionally, the high permeability, low coercive force, and relatively high saturation magnetization of these alloys have drawn special attention. In actuality, the iron content of the Ni-Fe system must be raised to satisfy the new requirements if a significantly higher saturation magnetization is needed for a particular application. Its performance as a soft magnetic material will be negatively impacted, nevertheless, as the rise in magnetocrystalline anisotropy with increased iron content causes both a drop in permeability and an increase in coercive force [2,3]. However, recent theoretical and

experimental findings [4–7] have demonstrated that nanostructuring can successfully lower a material's magnetocrystalline anisotropy constant. Further, the FeNi nanostructured material will have improved magnetic characteristics, such as increased permeability and reduced coercivity, in comparison to its polycrystalline version. Thus, it is believed that nanostructuring will offer an attractive solution to the disadvantage of increasing saturation magnetization in the Ni-Fe system. Additionally, it has been demonstrated that nanostructuring conventional materials can effectively increase their electrical resistivity [8,9] and mechanical hardness [6,10], which in the case of Ni-Fe alloys would improve both corrosion resistance and high-frequency performance by reducing eddy currents. Thus, nanostructuring is a practical and encouraging technique to enhance the Ni-Fe alloy system's magnetic characteristics. Mechanical milling considered a non-equilibrium nanostructuring method, enables the production of nanocrystalline structures by inducing complex microstructural transformations and crystalline defects such as dislocations and microstrains [11–14]. However, it is believed that the precise mechanism of the mechanical alloying process involves the repetitive welding and fracturing of powder particles during collisions between balls and between powder and containers. Interdiffusion over welded grain powder surfaces is how alloying then occurs. Mechanical alloying, as a process normally performed at temperatures below 673.15 K [15], has been used to suppress martensitic transformation and to obtain FCC γ-Fe-rich Fe–Ni alloys in the annealed condition [16,17]. On the other hand, it was observed that the concentration ranges of the BCC and FCC single-phase solid solutions depend on the milling intensity and shift to low nickel concentration at an increase in the milling intensity [12,18]. The final alloy structure is complexly affected by the milling intensity. As the intensity increases, two important factors change: the average temperature of the milling process rises on the one hand, and the concentration of various structural defects rises on the other. The FCC phase is less destabilized than the BCC phase due to the structural defects brought on by the MA [12]. According to the Fe–Ni phase diagram, a rise in milling temperature will stabilize the FCC structure and destabilize the BCC structure, as was previously mentioned [1]. Because of this, increasing the milling intensity will often decrease the range of BCC concentrations and expand the range of FCC concentrations. The concentration ranges of phase existence moved to the side of low nickel content after the samples were annealed at 923.15 K. Furthermore, for the Fe–Ni alloys made using the MA process, the effects of the FCC–BCC transformation temperature on composition have been examined [17,18]. It was discovered that, though to a lesser degree, the MA approach permitted the transition temperature to drop. It is still unclear exactly how this impact works. The small size of blocks in the MA FCC structure appears to be the primary reason of this transformation suppression temperature; nevertheless, structural defects like stacking faults and dislocations, as well as how they interact, might potentially be significant.

Many authors utilize X-ray diffraction analyses to validate their milling results, neglecting the complexity of mechanical synthesis in the dependence of nanostructuring on the defect structure characteristics and the relationship between the stability of the nanostructure and thermal heating. These features play a crucial role in determining the final properties of the materials [19]. Therefore, in-depth characterization will be necessary to understand the impact of the structure of the defects in terms of dislocations, microdeformations and the energy stored in the nanostructuring of the Ni-Fe alloy. Also, few studies have been devoted to the investigation of the thermal stability of this type of nanostructured alloy.

This study specifically focuses on the evolution of crystalline phases, particularly the formation of the FCC γ-(Ni-Fe) solid solution, also known as taenite, and the BCC α-(Fe-Ni) phase, referred to as kamacite, as well as the transformation of the α phase into γ upon an-

nealing [20]. The analysis of microdeformations and dislocations highlights the significance of crystalline defects in microstructural modifications, while the evaluation of stored energy offers insights into relaxation mechanisms and microstructural transformation processes. This work contributes significantly to the understanding of the mechanisms governing the evolution of nanocrystalline structures, paving the way for the design of Ni-Fe alloys with optimized properties suitable for advanced technological applications.

2. Materials and Methods

2.1. Materials

Pure elemental powders of nickel (Ni, purity~99.8%, particle size $\leq$ 30 μm; from Alpha Aesar) and iron (Fe, purity~99.9%, particle size $\leq$ 40 μm, from Alpha Aesar, Ward Hill, MA, USA), with respective particle sizes of 80 μm and 75 μm, were weighed separately and then mixed to obtain an equimolar composition (Ni-Fe), with a slightly higher amount of nickel. Mechanical alloying was carried out in a Retsch planetary ball mill (model PM400, Retsch, Haan, Germany) with milling times of 1, 2, 5, 10, 30, 40, 50, 60, 80, and 100 h at room temperature and under an argon atmosphere. The milling experiments were conducted with 10 g of powder mixtures in hardened steel jars containing five stainless steel milling balls with a diameter of 7 mm. The ball-to-powder weight ratio was set at 0.35, and the jar rotation speed was maintained at 400 revolutions per minute. To prevent powder adhesion to the walls of the container and the grinding balls, as well as to avoid powder agglomeration, the chosen milling sequence consisted of 2.5 min of milling followed by 5 min of rest. This sequence was applied to ensure optimal reproducibility of the milling process.

X-ray diffraction (XRD) measurements were performed using a Siemens D-500 diffractometer (Berlin, Germany) with Cu Kα radiation. Scans were collected over a 2θ range of 40–100°. A small angular step of 2θ = 0.02° and fixed counting times of 4 s were chosen to measure the intensity of each Bragg reflection. Crystallite size and lattice strain were calculated using Rietveld refinement with the X'Pert High Score Plus software (v5.3). To check the functional behavior of these alloys, it is necessary to obtain good refinements to stabilize the microstructure. The ratio of reliability parameters, represented as GoF (goodness of fit = Rwp/Rexp), gives information about the quality of fit, where Rwp and Rexp are the weighted residual error and the expected error, respectively. For the present study, best refinements were achieved when the GoF parameter varied from 1.06 to 1.13.

Morphology and composition studies were conducted using a scanning electron microscope (SEM) (DSM960A ZEISS, Carl Zeiss GmbH, Oberkochen, Germany) in secondary electron mode, operating at an accelerating voltage of 15 kV. The SEM was equipped with an energy-dispersive spectroscopy (EDS) analyzer (Vega Tescan, Brno, Czech Republic). A detailed analysis of particle size distribution was conducted using the segmentation method with the Trainable Weka Segmentation plugin in Image J software (version 1.x) [21,22].

Differential scanning calorimetry (DSC) was performed using a Mettler Toledo DSC822 device under an argon atmosphere, within a temperature range of 308 K to 973 K (35 to 700 °C), with a heating rate of 10 K/min. The milled powder was annealed in lidded ceramic crucibles under an argon atmosphere for 2 h at 923.15 K. Annealing was carried out in a Carbolite furnace with a heating rate of 15 K/min. After annealing, the samples were cooled in the furnace until they reached room temperature.

2.2. Theoretical

In our study, the X-ray diffraction patterns were analyzed using the Philips HighScore Plus software, which incorporates various methods for calculating diffraction peak profiles, including the Scherrer method, Williamson–Hall method, and Rietveld refinement [15].

Each peak was fitted with a pseudo-Voigt (PV) function, which is a linear combination of a Lorentzian (L) and a Gaussian (G) function (Equation (1)) [23]:

$$PV(2\theta) = \gamma L(2\theta) + (1-\gamma)G(2\theta) \quad (1)$$

where γ is an adjustable mixing parameter that describes the proportion of the Gaussian profile relative to the Lorentzian profile [9]. After removing the Cu Kα2 radiation contribution from the profiles, the average crystallite size <D> is calculated using the Scherrer formula (Equation (2)) [24,25]:

$$\langle D \rangle = \frac{k\lambda}{\beta_L \cos\theta} \quad (2)$$

where K is the shape factor, which varies depending on the crystal shape, λ is the wavelength of the CuKα1 radiation, θ is the Bragg angle, and β_L is the Lorentzian component of the peak width, related to the reduced crystallite size.

The average microstrain $\langle \varepsilon \rangle$ is calculated using the tangential formula (Equation (3)) [12,24]:

$$\langle \varepsilon \rangle = \frac{\beta_G}{4\tan\theta} \quad (3)$$

where β_G is the Gaussian component of the peak broadening, resulting from microstrain present in the material.

For the Rietveld method, the average values of crystallite size <D> and strain $\langle \varepsilon \rangle$ are determined by analyzing the broadening of diffraction peaks as a function of the diffraction angle. This formula in (Equation (4)) is used to fit the parameters D and ε so that the theoretical model best matches the experimental data:

$$\beta = \frac{K\lambda}{D\cos\theta} + 4\varepsilon\tan\theta \quad (4)$$

where β is the total peak broadening (in radians) at full width at half maximum (FWHM), K is the shape factor (or Scherrer constant, typically between 0.9 and 1), λ is the wavelength of the X-ray radiation, D is the average crystallite size, θ is the Bragg angle, and ε is the microstrain in the material.

Using the intensities of the fitted peaks, HighScore-Plus calculates the relative percentage of each phase present in the sample through a quantitative analysis method based on the integral intensity of the diffraction peaks. This method is based on the principle that the net area of the peaks in the diffraction pattern is proportional to the amount of each phase. The formula used to determine the relative percentage of a specific phase is as follows:

$$\%\ phase = \frac{I_{\text{total}}}{I_{\text{phase}}} \times 100 \quad (5)$$

where I_{phase} is the integrated intensity of the peak corresponding to a specific phase, and I_{total} is the sum of the integrated intensities of all peaks. By accounting for calibration factors and experimental conditions, HighScore-Plus enables the precise quantification of the phases. These results are critical for interpreting crystallographic data and understanding the material properties of the sample.

3. Results

3.1. Morphological Analysis

Figure 1 presents the SEM micrographs of the FeNi sample mixtures obtained after 1, 5, 10, 20, 40, 60, and 100 h of milling time. The milling times up to 100 h result in a considerable reduction in particle size after the extended milling time, depending on the

composition of the powder mixture and the dominant compressive forces. Due to ball–ball and ball–wall collisions, the ductile powders are first crushed by compressive forces to form fine particles (2 h milling). Then, for periods ranging from 5 to 20 h, agglomerated particles develop by cold welding and coalescence of the powder particles. As the milling process progresses up to 40 h, the powder particles tend to fracture again. This is because the powder particles harden due to work hardening caused by severe plastic deformation during the continuous milling, which eventually causes particle fracture. This phenomenon becomes more pronounced for higher milling times.

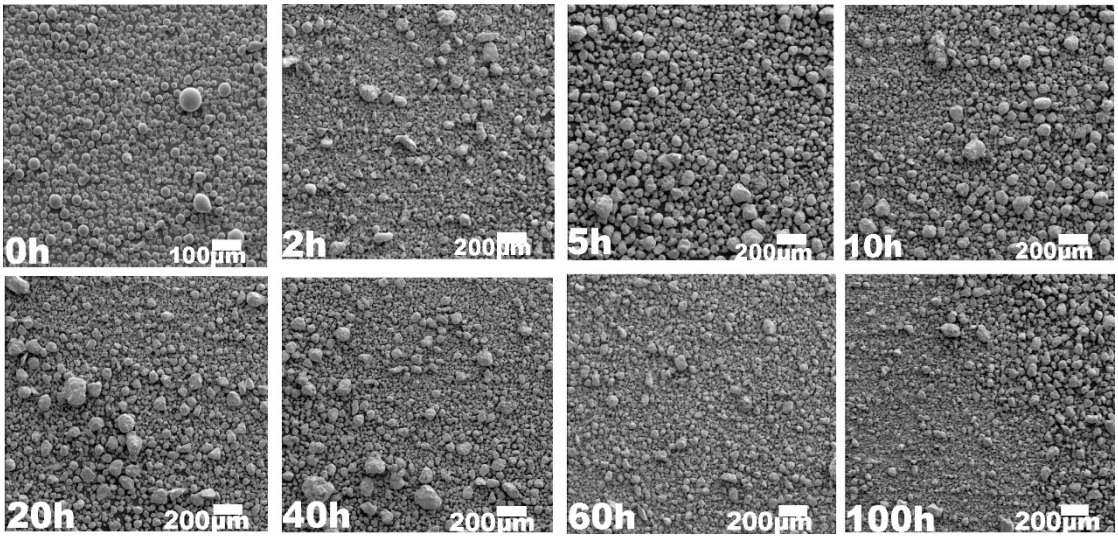

Figure 1. SEM image obtained after selected milling times, up to 100 h.

Figure 2 gives us more precise information on the evolution of the particle size as a function of milling time. For the unmilled powder mixture, a single population of particles is observed with a size value of 95 µm. After 2 h of milling, a slight decrease in size is observed to a value of approximately 55 µm. Increasing the milling time up to 5 h results in a significant increase in size up to the value of 120 µm. Subsequently, going from 10 to 40 h of milling, although the size distribution appears heterogeneous, the average particle size varies from 100 µm after 10 h to 65 µm for the 40 h of milling. For longer milling times, a decrease in the particle size is observed to the average value of around 20 µm after 60 h. This size distribution continues until the end of milling at 100 h. As a result, these various states of powders showed that particle size may become larger, corresponding to particles agglomerated by cold welding, or smaller following fracturing, after hardening by the dominant compressive pressures or by the effect of solid solutions. Additionally, extremely fine and larger particles can be re-fused, increasing the size, thanks to the atomically pristine surfaces produced during fracture.

The EDS spectra recorded after 10, 20, 40, and 100 h of grinding are presented in Figure 3. They show the absence of oxygen and the presence of mixed nickel and iron, confirming that no contamination of the jars or oxygen impurities was observed. These observations highlight the importance of controlling milling conditions to optimize particle size reduction while maintaining essential properties such as compactness and flowability.

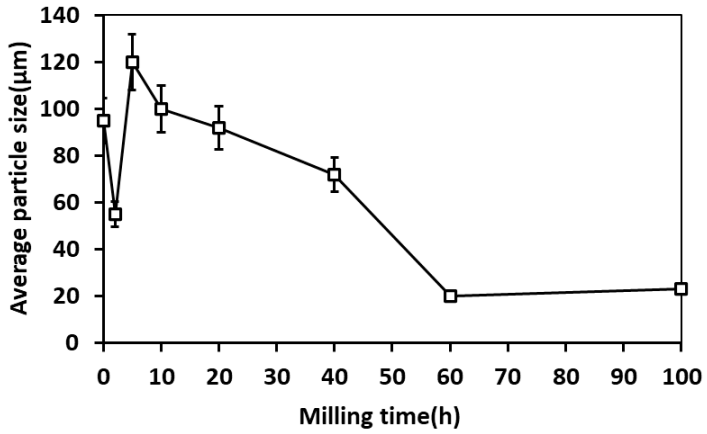

Figure 2. Evolution of particle size as a function of selected milling times.

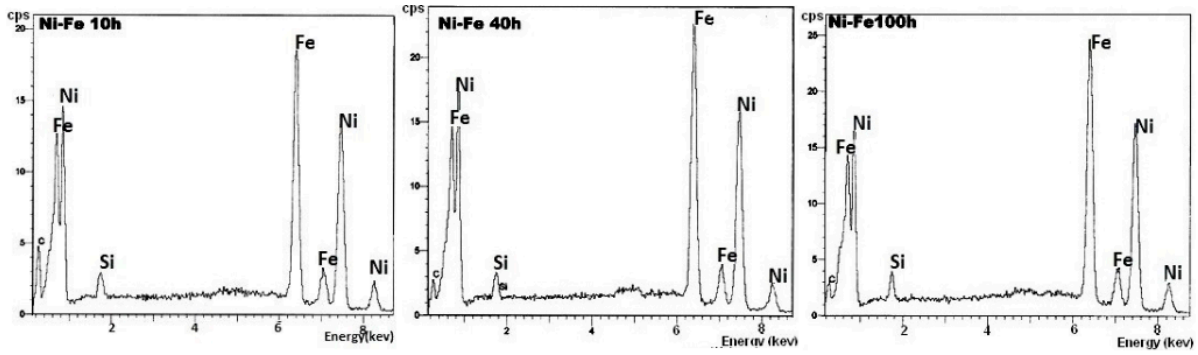

Figure 3. Evolution of particle morphology after 10, 40, and 100 h of milling.

3.2. Structural and Microstructural

3.2.1. Structural and Phase Proportions

Figure 4 illustrates the evolution of X-ray diffraction (XRD) patterns as a function of the milling time of Ni-Fe powders, using CuKα radiation. The XRD spectra of the initial powders (0 h of milling) show reflections corresponding to the BCC α-Fe metal (space group Im-3m; a = 2.8650(2)) and FCC-Ni (space group Fm-3m; a = 3.522(1) Å). After 2 h of milling (2 h), the reflection peaks (200) and (211), associated with the elemental BCC α-Fe and FCC-Ni phases, disappear. Iron atoms dissolve into the nickel lattice, leading to the formation of an FCC γ-(Ni-Fe) solid solution (taenite, PCD code 534829, $Fe_{0.4}Ni_{0.6}$) and the incorporation of nickel into the α-iron matrix to form the BCC α-(Fe-Ni) phase (kamacite, PCD code 456555, $Fe_{0.95}Ni_{0.05}$).

These observations are consistent with the findings of Kaloshkin et al. [25]. During the first 30 h of milling, the BCC phase decreases drastically (from 31.3% to 16.9%) (Figure 5), while the proportion of the FCC phase increases from 68.7 to 83.1%. This preferential transformation from the BCC to FCC structure is attributed to the mechanical stresses generated during milling, which introduce numerous crystalline defects (vacancies, dislocations. . .) that promote the nucleation and growth of FCC nuclei, which are energetically more stable. Beyond 30 h of milling, the proportion of the FCC phase continues to increase, reaching 90.3% after 100 h, though the BCC phase, while minor, persists with a percentage of 9.7%. Many authors have found the same result for two-phase systems with extended milling times. Our results are consistent with published data, especially with the data reported by refs. [12,14,26,27]. The low-temperature phase relations are still subject to some limitations despite the extensive research, mostly because it is challenging to achieve a stable equilibrium at temperatures lower than roughly 573.15 (K) [28]. Furthermore, Fe-Ni is a classic illustration of the interplay between structural and magnetic ordering that influences phase

equilibria [29,30]. However, the final alloy structure is complicatedly affected by the milling intensity; as the intensity increases, two primary factors change: the average temperature of the milling process rises on the one hand, and the concentration of various structural fault types increases on the other.

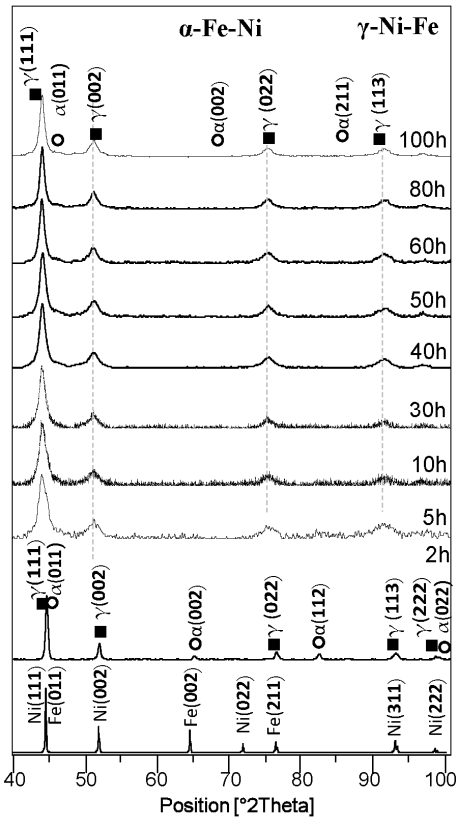

Figure 4. X-ray diffraction (XRD) patterns as a function of the milling time of Ni-Fe powders.

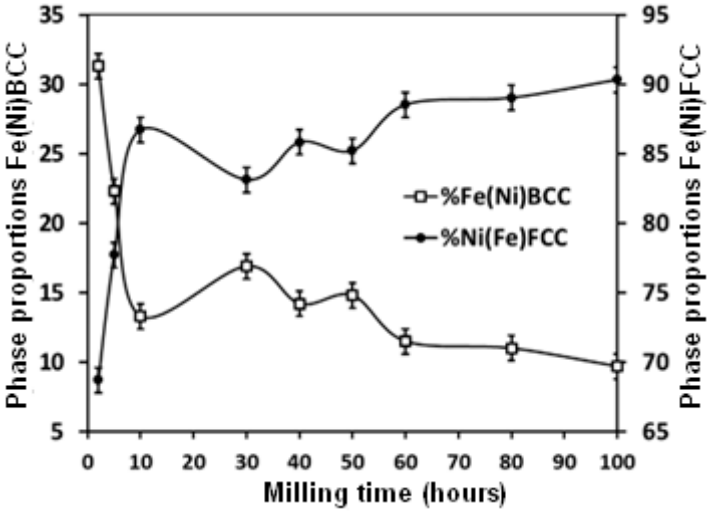

Figure 5. Evolution of the phase proportions as a function of milling time.

The high-angle diffraction lines gradually broaden until their complete disappearance. The variations observed in the FWHM values highlight the complex effects of mechanical milling on Ni-Fe alloys, confirming that excessively long milling times can compromise the desired properties [31].

3.2.2. Lattice Parameters

Figure 6 presents the lattice parameters, a, for FCC γ-Ni(Fe) as a function of milling time. It was observed that between 2 and 5 h of milling, the lattice parameter increased from 3.5228(1) Å to 3.5767(1) Å, indicating a variation of Δa = 0.0538 Å. Simultaneously, the position of the diffraction peak is shifted from 44.523 to 43.934°, as shown in Figure 4. This increase in the lattice parameter suggests that milling induces an expansion of the crystal lattice, resulting from the mechanical energy applied, which promotes the formation of a new FCC γ-Ni-Fe solid solution. Between 5 and 30 h of milling, the lattice parameter slightly decreases from 3.5760(1) to 3.5740(1) Å, showing a trend toward stabilization. However, the peak position continues to decrease, reaching 43.916°. This variation indicates that the crystal lattice is still undergoing modifications, which can be attributed to an increase in crystalline defects and the dilation of interatomic distances.

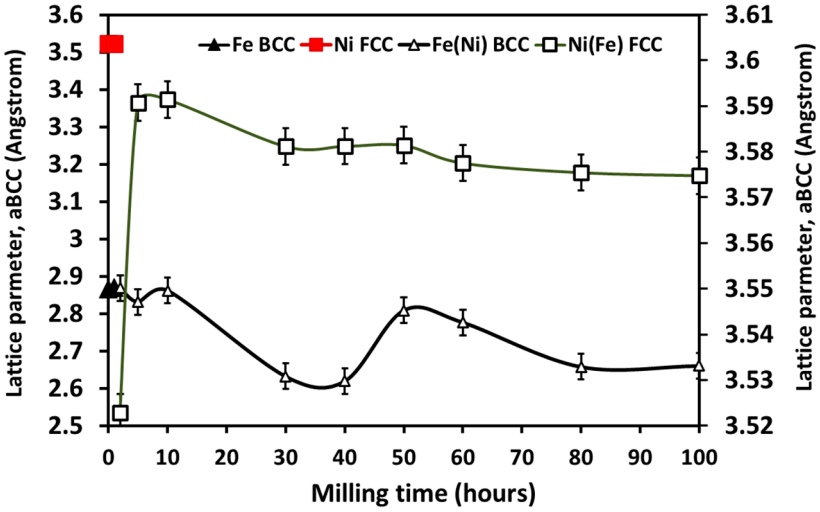

Figure 6. Evolution of the lattice parameters as a function of milling time.

On the other hand, during the initial hours of milling, the BCC lattice parameter decreased from 2.8688(2) (2 h) to 2.8316(1) Å (5 h). This slight decrease (−0.072 Å) in the lattice parameter can be explained by considering the small difference in the atomic radii of Fe and Ni atoms, which are 0.126 and 0.124 nm, respectively [1,28]. The applied mechanical energy promotes the incorporation of nickel into the BCC α-Fe matrix to form the BCC α-(FeNi) phase, with a space group Im-3m. Between 5 and 30 h, the lattice parameter continues to decrease, reaching a minimum of 2.6325(1) Å at 30 h. This significant variation may indicate a restructuring of the crystalline lattice. The lattice parameter initially increases with the rising nickel content, reaching a maximum of approximately 13 at.% Ni, before decreasing to between 13 and 30 at.% Ni [32,33]. After reaching this minimum, the lattice parameter begins to slightly increase, reaching 2.8090(1) Å at 50 h. This increase may suggest atomic rearrangement. At this stage, a recrystallization process likely promotes the reorganization of atoms to form a more stable structure. Beyond 60 h, the parameter stabilizes and oscillates around similar values (approximately 2.66 Å), indicating that the material begins to approach an equilibrium state after prolonged milling. During the formation of the BCC α-(Fe-Ni) phase, the variation in peak positions is influenced by a dynamic process governed by initial fragmentation and defects formation, followed by recrystallization and structural equilibration. These processes result in modifications to interplanar distances, causing the diffraction peaks to shift toward higher angles [34]. On the other hand, during the initial hours of milling, the BCC lattice parameter decreases from 2.8688(2) (2 h) to 2.8316(1) Å (5 h). This initial reduction can be attributed to the fragmentation of crystallites. The applied mechanical energy promotes the incorporation of nickel into the α-iron matrix

to form the α-(Fe-Ni) phase, with a space group Im-3m. Between 5 and 30 h, the lattice parameter continues to decrease, reaching a minimum of 2.6325(1) Å at 30 h. This significant variation may indicate a restructuring of the crystalline lattice.

3.2.3. Crystallite Sizes

The evolution of FCC γ-(Ni-Fe) crystallite sizes is illustrated in Figure 7b. The initial crystallite sizes are 57.36 nm and 59.79 nm for Ni and Fe, respectively, with low full width at half maximum (FWHM) values of 0.2364° and 0.3267° for the $(111)_{FCC}$ and $(110)_{BCC}$ reflections, respectively.

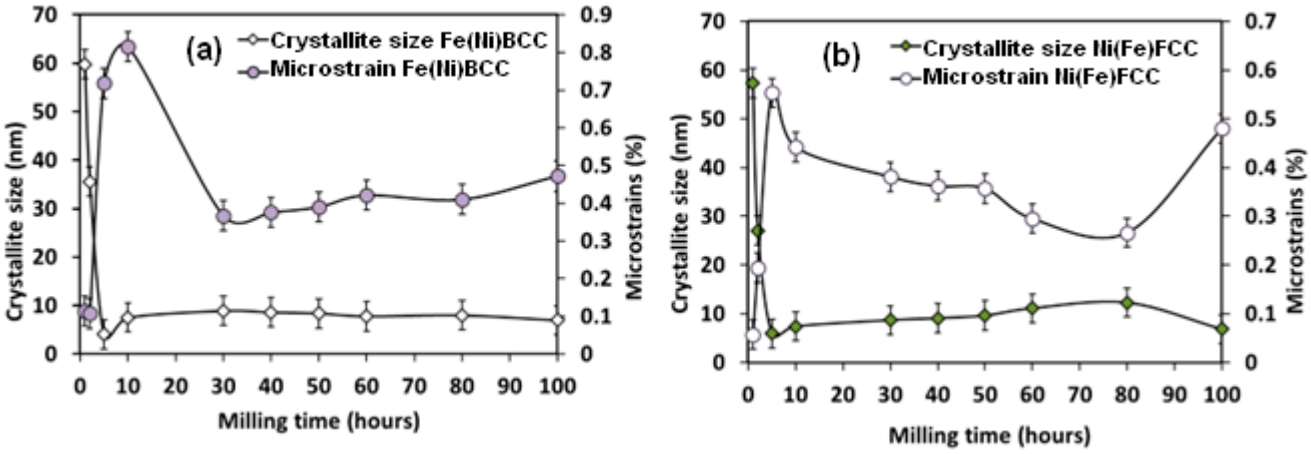

Figure 7. Evolutions of the crystallite size and microstrain values of (**a**) BCC-FeNi and (**b**) FCC-NiFe as a function of milling time.

After 5 h of milling, a significant reduction in crystallite size is observed due to the high rate of fracture and plastic deformation. The crystallite size is reduced to 6 nm for the FCC γ(Ni-Fe) structure and 5 nm for the BCC α(Fe-Ni) structure, with corresponding FWHM values of 1.610° for $(111)_{FCC}$ and 2.557° for $(110)_{BCC}$. These results are consistent with previous studies that reported similar reductions in grain size during mechanical milling [35]. At 10 h, the crystallite size of FCC γ-(Ni-Fe) increases to 7.4 nm, although the relatively high FWHM suggests an accumulation of defects within the material. This observation aligns with findings from other studies on Ni-Fe alloys [11]. After 30 h of milling, the FWHM decreases to 1.139°, and the FCC crystallite size increases to 8.66 nm, indicating an improvement in crystalline quality. However, beyond 40 h, although the crystallite size reaches 9.06 nm, the FWHM slightly decreases to 1.060° for $(111)_{FCC}$, signaling the accumulation of defects and disruption in crystalline properties. At 60 h, the crystallite size reaches a maximum of 11.09 nm with a reduced FWHM of 0.864°. These results are consistent with those obtained using a planetary ball mill (P7 type) operating at 500 rpm, which produced crystallite sizes of approximately 11 nm after 50 h [36]. Therefore, this 60 h milling duration appears sufficient to achieve a stable FCC crystalline structure. However, at 80 h, despite a maximum crystallite size of 12.26 Å, the FWHM increases to 1.40°, suggesting that prolonged milling may lead to excessive fragmentation and structural degradation of the crystallites. In conclusion, a milling duration of 60 h is optimal for preserving the microstructural integrity of the Ni-Fe FCC phase while achieving a stable crystalline structure.

The analysis of the evolution of crystallite sizes for the BCC Fe(Ni) alloy, also shown in Figure 7a, reveals a complex dynamic as a function of milling duration. The crystallite size initially increases from 5 nm to 7.5 nm between 5 and 10 h. Simultaneously, the FWHM varies, increasing from 2.58° to 3.084° during this period, indicating an accumulation of defects. However, the diffraction peak (110) remains relatively broad even after 100 h

of milling, with a crystallite size of 7 nm. Theoretically, variations in crystallite size and FWHM are directly related to milling time, emphasizing that the BCC compound undergoes structural disturbances and does not reach equilibrium in its structure. This crystallite size value is lower than the 16.5 nm obtained for ultrafine iron-nickel particles with a similar composition prepared by the gas condensation method [36,37].

3.2.4. Lattice Strains

Lattice strains refer to local variations in interplanar distances, d − Δd and d + Δd, caused by non-uniform crystalline distortions. These distortions are generated by crystalline defects or by the formation of new solid solutions. The analysis of the evolution of microstrain in Ni-Fe alloys as a function of milling time, shown in Figure 7b, reveals that at 5 h, the microstrain for the FCC phase is 0.55%, while for the BCC phase it is 0.71% (Figure 7a). As milling continues to 10 h, the microstrain for the FCC phase decreases to 0.442%, while for the BCC phase it increases to 0.815%, suggesting that milling has a more pronounced effect on the BCC structure in terms of deformation. By 30 h, the microstrain for the FCC phase continues to decrease to 0.381%, while that of the BCC phase drops to 0.367%, indicating stabilization or improvement in the FCC structure. At 40 h, the microstrain values converge, with 0.362% for the FCC phase and 0.376% for the BCC phase, showing that both structures undergo slight modifications under prolonged milling. For the extended milling time up to 100 h, the microstrain for the FCC phase slightly increases to 0.480%, while that of the BCC phase decreases to 0.472%. These results demonstrate that prolonged milling induces complex variations in the microstructure of Ni-Fe alloys. Although the BCC structure initially exhibits higher microstrain, the stabilization of the FCC structure suggests it may possess superior long-term mechanical resilience under milling conditions [38].

3.3. Structure of Defects Analysis

3.3.1. Dislocation Density

For the milled samples subjected to severe plastic deformation, dislocations are the primary source of microstrains in the crystalline system near the grain boundaries. The dislocation density can be expressed using Equation (6) as follows:

$$\rho = \rho_{fcc} + \rho_{bcc} \tag{6}$$

In general, the dislocation density, ρ_s can be expressed as a function of the lattice strain (ε) and the crystallite size, D, using the following Equation (7) [35,39,40]:

$$\rho_s = \frac{2\sqrt{3} \times (\varepsilon)^{1/2}}{D \times b} \tag{7}$$

where the Burgers vector of dislocations, b, is equal to $a_{fcc}\ \frac{\sqrt{2}}{2}$ for the γ-Ni(Fe) FCC structure and $a_{bcc}\ \frac{\sqrt{3}}{2}$ for the α-(Fe-Ni) BCC structure.

The lattice parameters a_{fcc} and a_{bcc} are adjusted as a function of milling time for the FCC γ-Ni(Fe) and BCC α-(Fe-Ni) structures, respectively. Thus, the dislocation density ρ_s can also be represented by Equation (8) as follows:

$$\rho_s = 2\sqrt{3} \times \left[\left(\frac{\varepsilon}{Db} \right)_{fcc} + \left(\frac{\varepsilon}{Db} \right)_{bcc} \right] \tag{8}$$

Figure 8 illustrates the evolution of dislocation density (ρ_s) within the Ni-Fe compound as a function of milling duration. Initially, a peak in dislocation density is observed at the early stage of milling, specifically at 5 h, with a value of $1.9 \times 10^{17}\ m^{-2}$. These defects result

from grain deformation and dislocation slip. Following this intense peak, the dislocation density gradually decreases at 10 h of milling (10 h), reaching approximately 1.168 × 10^{17} m^{-2}. This reduction is attributed to dynamic annealing phenomena, where dislocations partially annihilate under the milling mechanism. The system reaches an equilibrium state between 30 and 80 h of milling, with values stabilizing in the range of 6.14 × 10^{16} to 5.35 × 10^{16} m^{-2}. However, at the end of the milling process, the dislocation density increases again, reaching 9.93 × 10^{16} m^{-2} after 100 h of milling. This complex evolution can be attributed to several factors, including dynamic annealing, the accumulation of defects, and the fact that the rate of new dislocation creation exceeds the rate of annihilation. Additional contributions are primarily derived from structural and compositional irregularities in the grain boundary (GB) regions compared to the interior of the grains.

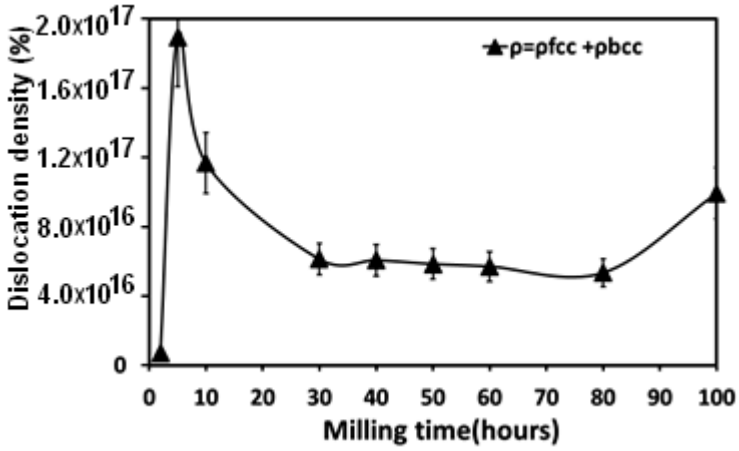

Figure 8. Evolution of the dislocation density values as a function of milling duration.

3.3.2. Stored Energy E_{st}

In plastically deformed materials, the theoretical estimation of the stored energy (Es) is proportional to the dislocation density (screw and edge dislocations) per unit volume in the material, as defined by the following Equation (9) [41,42]:

$$E_{st} = \beta \times \rho_s \quad (9)$$

where ρ_s is the dislocation density and β is the proportionality coefficient [43,44], given by the Equation (10):

$$\beta = AGb^2 \times In\frac{R}{r} \quad (10)$$

Here $A = \frac{1}{4\pi}$ for screw dislocations and $A = \frac{1}{4\pi(1-\sigma)}$ for edge dislocations. σ refers to Poisson's ratio and equals 0.3 for Ni-Fe alloys. G refers to the shear modulus for Invar Fe-Ni36 alloy and is equal to 58 × 10^{10} N/m^2. The proportionality coefficient β was estimated to be 171 × 10^{-10} N, allowing the calculation of the stored energy (E_{st}) per mole in the mechanically alloyed (MA) samples according to the relationship in (Equation (10)) (Figure 9). The evolution reveals a significant increase between 2 h and 5 h of milling, rising from 1.22 × 10^{17} J/m^3 to 3.23 × 10^{18} J/m^3. This evolution reflects the early stages of the milling process, characterized by the formation of a large number of dislocations, accompanied by a notable increase in the specific surface area of the Ni-Fe compound [45]. Between 30 h and 80 h, the stored energy values reach a plateau, fluctuating slightly around 1.05 × 10^{18} to 9.15 × 10^{17} J/m^3. At this stage, various mechanisms, such as dislocation motion, annihilation, and crystalline structure reorganization, operate synergistically to reduce the internal stresses induced by dislocation formation. These dynamic relaxation processes maintain structural equilibrium, thereby ensuring mechanical stability and mate-

rial performance [46,47]. However, beyond 100 h of milling, a renewed increase in stored energy is observed, reaching 1.70×10^{18} J/m^3. This behavior suggests an interruption in the dynamic relaxation mechanisms. This change could be attributed to phenomena such as recrystallization or an increased accumulation of crystalline defects.

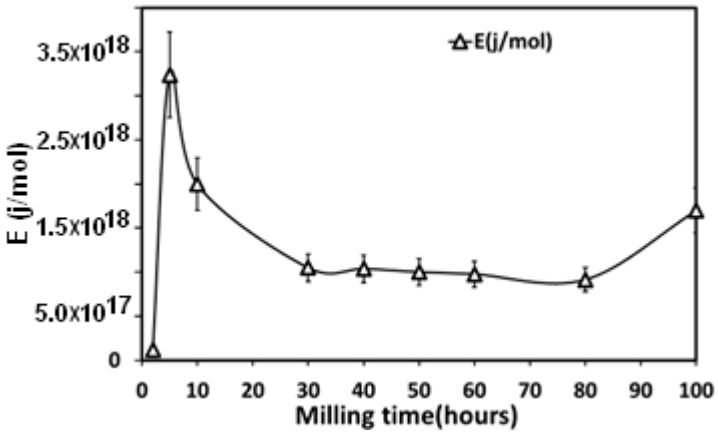

Figure 9. Evolution of the stored energy values as a function of milling duration.

3.4. Thermal Stability Analysis

3.4.1. DSC Analysis

The study of the thermal behavior of milled samples is essential for selecting appropriate annealing temperatures to avoid recrystallization [48]. Figure 10 presents the thermograms obtained at a heating rate of 10 K/min.

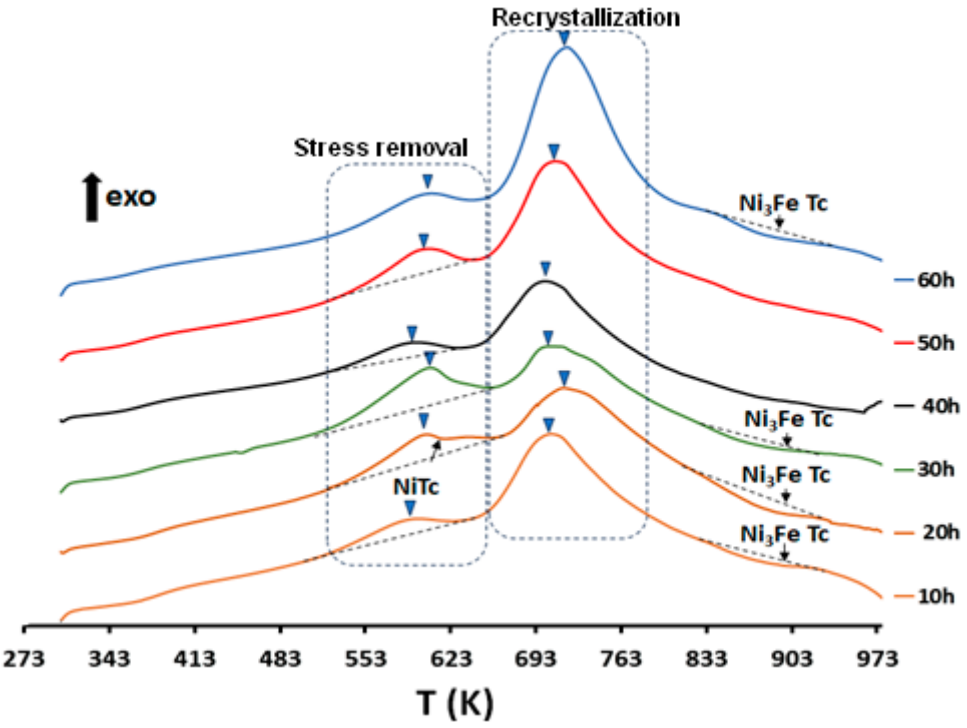

Figure 10. Thermograms obtained as a function of milling duration at a heating rate of 10 K/min.

The two exothermic peaks identified by differential scanning calorimetry (DSC) correspond to two successive relaxation mechanisms. The first broad peak, located in the range [583.15 K–601.15 K], reflects structural relaxation. The evolution of this peak's intensity as a function of milling time indicates that the relaxation is primarily attributed to the stresses

generated by dislocation formation. It increases proportionally with the milling duration. A rapid increase in ΔH_1 is observed, reaching a maximum of 10.35 J/g after 30 h of milling, indicating the release of significant energy as the material returns to an equilibrium state (Figure 11). The second broad peak, located in the range [702.15 K; 733.15 K], is more intense and reflects complex processes such as defect redistribution, phase transformations, and advanced recrystallization. The increase in dislocation density leads to a rise in internal energy due to the elastic stress fields generated by these defects. These stresses influence thermal relaxation mechanisms. The stored enthalpy, represented by ΔH_2 (Figure 11), shows an increase up to 59.54 J/g after 60 h of milling, before gradually decreasing with the material's microstructural refinement. This behavior is consistent with similar observations reported for other single-crystal systems prepared by milling [48,49]. Moreover, the temperature associated with the ΔH_2 peak increases with milling time, indicating that thermal processes occur at higher temperatures due to the accumulation of internal energy from crystalline defects. This shift reflects modifications in the underlying thermodynamic mechanisms, directly linked to the material's microstructural evolution during milling.

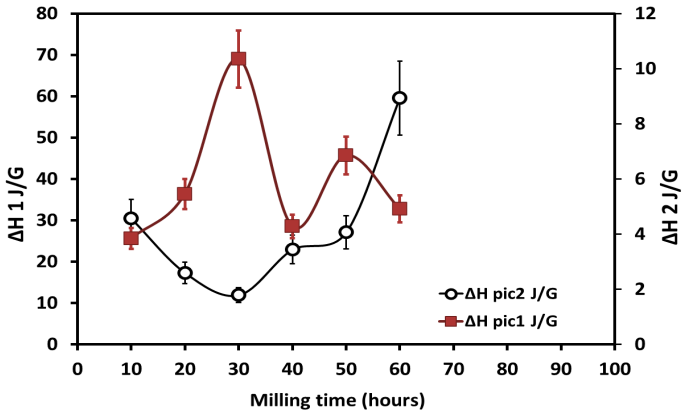

Figure 11. The stored enthalpy obtained as a function of milling duration at a heating rate of 10 K/min.

Phase evolution is also observed in the DSC thermograms. For the sample milled for 5 h, an endothermic peak is detected at 613.15 K, corresponding to the Curie temperature of nickel, indicating the initial presence of this phase. However, for milling durations exceeding 10 h, this transition disappears, suggesting the complete transformation of nickel into a Ni-Fe solid solution. The formation of this solid solution is confirmed by the appearance of a second endothermic peak at 873.15 K, attributed to the Curie temperature of Ni_3Fe (Figure 10). X-ray diffraction (XRD) analyses corroborate the formation of this solid solution.

3.4.2. Structural Analysis

Initially, the milled compound consists of a major FCC γ-Ni(Fe) phase (PCD database code: 453083, $Ni_{0.82}Fe_{0.18}$, "taenite") and a minor BCC α-(Fe-Ni) phase (PCD database code: 534803, $Fe_{0.6}Ni_{0.4}$, "kamacite"). XRD results for the sample milled for 1 h and annealed at 923.15 K reveal the presence of two phases (Figure 12). The major phase is FCC γ (Fe-Ni), constituting 95.9% of the material. The minor phase is α-Ni(Fe) with a BCC structure, representing 4.1%. After 10 h of annealing (10 h + TTH), X-ray diffraction (XRD) patterns reveal characteristic peaks of the FCC γ-Fe(Ni) phase (database code: PCD 312469, composition $Fe_{0.68}Ni_{0.32}$). Simultaneously, peaks associated with the BCC α-(Fe-Ni) phase disappear.

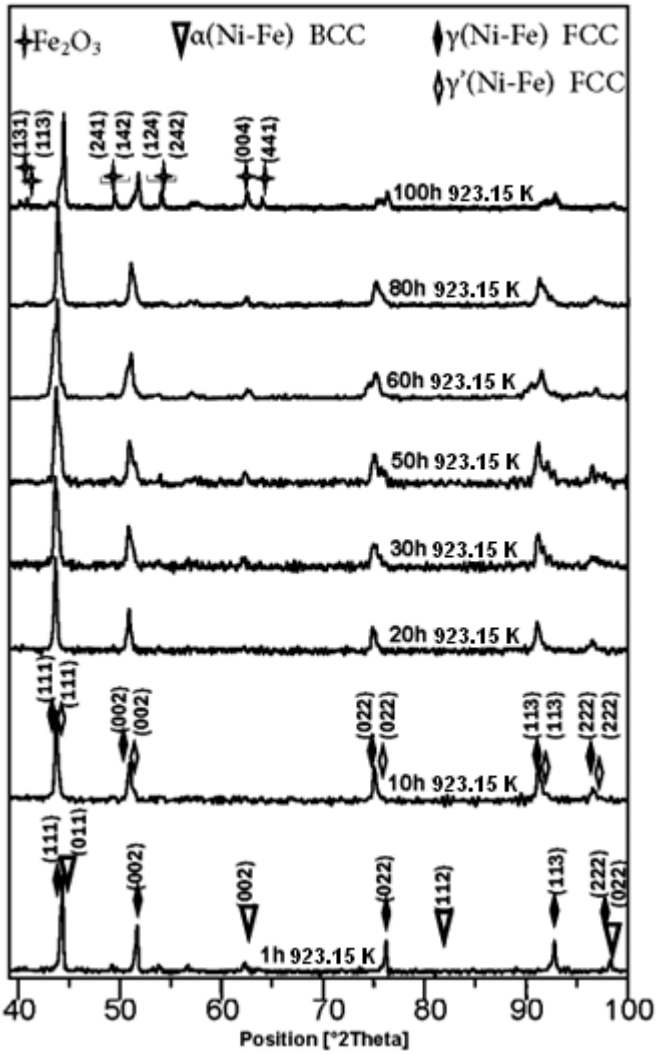

Figure 12. XRD patterns of the samples milled for selected times then annealed at 923.15 K for 2 h.

During the annealing of Fe-Ni alloys, an allotropic transformation is commonly observed. This phenomenon can be attributed to the substitution of Ni atoms within the α-Fe structure, including at grain boundaries and dislocation zones. This substitution leads to the formation of the FCC γ'-(Ni-Fe) phase (database code: PCD 454950, $FeNi_3$). This behavior highlights that the γ'-phase results from the transformation of the α-phase ($\alpha \rightarrow \gamma'$). The evolution of the phase proportions obtained for the milled powders annealed at the temperature of 923.15 K for 2 h are presented in Figure 13. Additionally, an Fe_2O_3 oxide phase, characterized by the low-intensity peaks labeled (131), (113), (241), (142), (124), (004), and (441), was detected. This suggests later contamination by oxide during annealing. This phenomenon has been observed in similar contexts, as reported in previous studies [48,50,51].

The thermal agitation generated during annealing at 923.15 K causes atom segregation at grain boundaries and the gradual diffusion of dislocations, leading to a modification in lattice composition and structural variation in the crystal network. This transition drives unstable phases at this temperature toward a more stable solution. Consequently, a variation in the lattice parameter is observed as shown in Figure 14; a significant increase in the lattice parameter is observed for short milling durations (1 h to 20 h). The initial BCC α-Fe(Ni) phase, with a lattice parameter of a = 2.8665(1) Å, transforms into a FCC γ-Ni(Fe) phase, with a lattice parameter of approximately a = 3.5743(1) Å. At 923.15 K, atoms possess

sufficient mobility to reorganize, promoting nickel diffusion into the iron lattice facilitated by the similarity of their atomic radii [1].

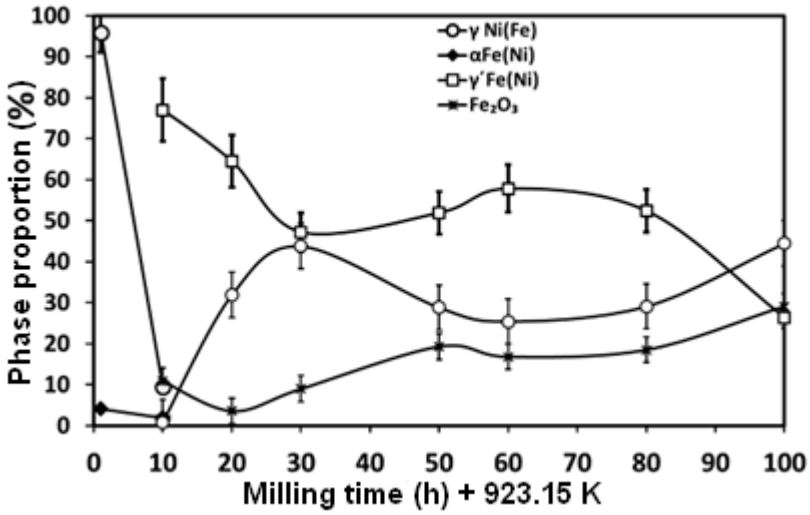

Figure 13. Evolution of the phase proportions obtained for the milled powders annealed at a temperature of 923.15 K for 2 h.

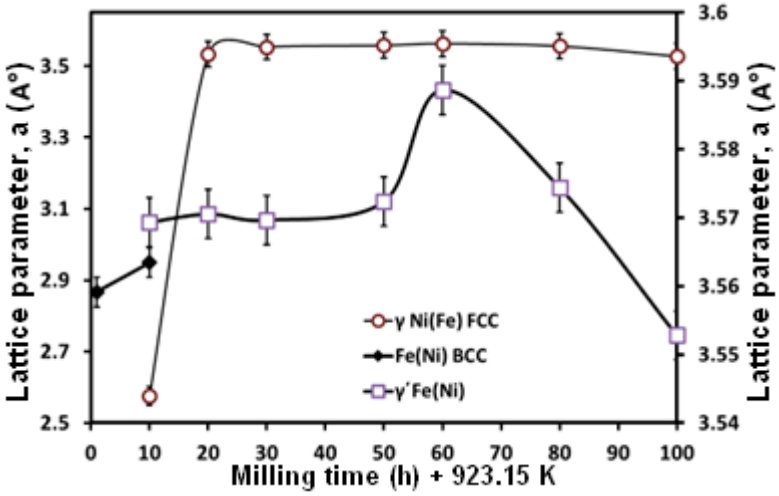

Figure 14. Evolution of the lattice parameters obtained for the milled powders annealed at a temperature of 923.15 K for 2 h.

For longer milling durations (from 30 to 80 h), followed by annealing at 923.15 K, the lattice parameter stabilizes, fluctuating between 3.5628(1) Å and 3.5536(1) Å. This indicates that the solid solution approaches its equilibrium composition at an annealing temperature of 923.15 K [19]. For samples milled for 100 h and annealed at 923.15 K, annealing induces atom reorganization, resulting in a more compact structure and, consequently, a lower lattice parameter of 3.5273(1) Å [19]. Annealing at 923.15 K also promotes internal stress relaxation, leading to better crystal network organization and atom diffusion, accompanied by the elimination of point defects, as noted by [48]. The variation in lattice parameters after annealing is more pronounced for longer milling times due to the higher accumulation of defects and internal stresses during milling. For instance, after 100 h of milling followed by annealing at 923.15 K, the variation in the lattice parameter is 0.0475 Å, compared to only 0.0147 Å for 60 h of milling. This illustrates the increasing impact of internal stresses on the crystalline structure with extended milling durations.

3.4.3. Microstructural Analysis

The analyzed variations in crystallite size and microstrain as a function of milling duration and annealing at 923.15 K for 2 h are presented in Figure 15, providing insights into the combined effects of mechanical deformation followed by thermal treatment on the γ-Ni(Fe) and γ′-FeNi phases. This present study confirms the structural stability of the FCC γ-Ni(Fe) phase, which is present both before and after annealing at 923.15 K. For a milling duration of 10 h, the initial crystallite size is 58.03 nm, which decreases significantly to 8 nm after annealing, indicating effective recrystallization. For 30 h of milling, the crystallite size decreases from 17.5 nm before annealing to 9 nm after treatment, representing a reduction by half. Samples subjected to 50 h and 60 h of milling also show notable reductions in crystallite size: from 16 nm to 10 nm and from 14.5 nm to 12 nm, respectively. Conversely, for 80 h of milling, the crystallite size slightly increases after annealing, from 17.66 nm to 12.26 nm, with a negative variation of −5.4 nm. Finally, for 100 h of milling, the initial crystallite size is 49.36 nm and decreases to 6.82 nm [52].

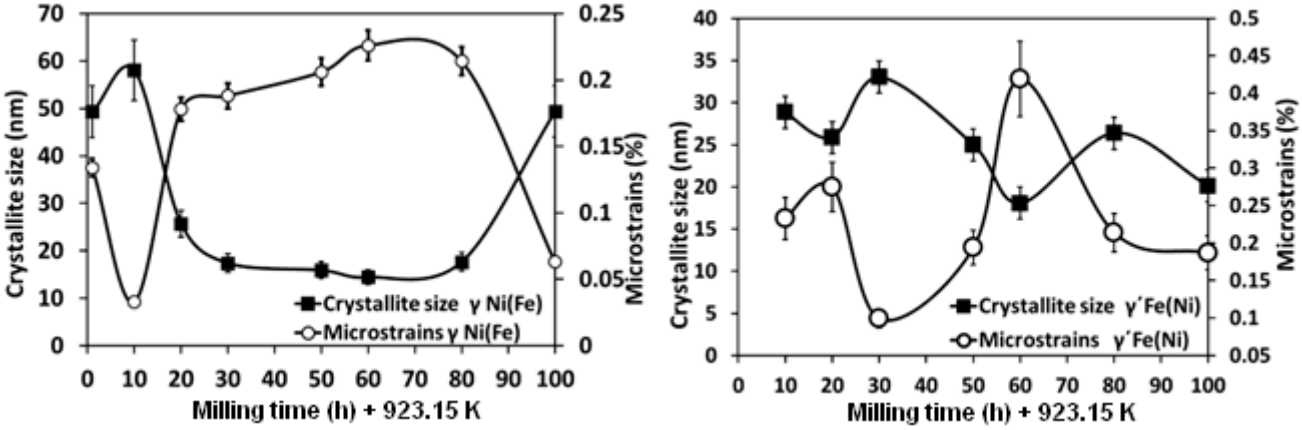

Figure 15. Evolution of the microstructural parameters (crystallite size and microstrain) obtained for the milled powders annealed at a temperature of 923.15 K for 2 h.

The analysis of crystallite size variations for the γ′-FeNi compound after annealing at 923.15 K highlights complex results associated with structural modifications and allotropic transitions, particularly the $\alpha \rightarrow \gamma$ phase transformation occurring during annealing. The data reveal significant variations in crystallite size before and after thermal treatment, depending on the milling duration. For instance, with 10 h of milling, the crystallite size decreases from 57.36 nm to 28.85 nm, reflecting a reduction of 28.51 nm. Conversely, certain samples exhibit an increase in crystallite size, as optimal annealing temperatures promote grain growth by facilitating grain boundary movement and coarsening [51–53]. For example, a milling duration of 30 h shows a marked increase in crystallite size, from 8.66 nm Å to 33.03 nm. This increase is enabled by annealing at 923.15 K, which promotes atomic mobility. In contrast, for longer milling durations, such as 50 and 60 h, the crystallite sizes after annealing reach 25 nm and 18.06 nm, respectively, with more moderate variations. Finally, samples subjected to extended milling durations (80 and 100 h) continue to show positive increases in size after annealing, confirming the influence of thermal and structural mechanisms on structural evolution. The work of Kaloshkin et al. [54] on phase transformations in the Fe-Ni system during mechanical milling and annealing demonstrated that in the case of $Fe_{75}Ni_{25}$ produced by mechanical milling and annealed at 923.15 K, with grain sizes ranging from 35 to 50 nm, the γ′ phase can remain stable at room temperature. These findings support our hypothesis that oxidation significantly delays the martensitic transformation, contributing to the stability of the γ phase when the grain size exceeds a critical threshold [20].

On the other hand, after annealing at 923.15 K for 2 h, the diffraction lines become sharper and more symmetrical, reflecting structural relaxation. This leads to a reduction in microstrain, regardless of the initial milling duration. At favorable temperatures, atoms have sufficient mobility to reorganize, thereby reducing the stored strain energy within the material. However, some residual microstrain persists, suggesting that certain stresses are not fully relaxed at 923.15 K. This phenomenon decreases the density of randomly distributed dislocations and reduces internal microstress, thereby improving short-range structural order within the Ni-Fe alloy. At 5 h of milling plus annealing (5 h + annealing), the microstrain was measured at 0.233% for FCC γ'-Fe(Ni), indicating significant structural transformation. Annealing processes can induce structural relaxation and recrystallization, which reduce dislocations and microstrain. This behavior is like the recrystallization and stabilization observed in Fe-Ni alloys [44]. After 30 h followed by annealing, the microstrain drops to 0.099%, which can be attributed to atomic motion and recrystallization eliminating the dislocations accumulated during milling. Conversely, for prolonged milling durations, microstrain exhibits a complex variation: it increases to 0.194% after 50 h followed by annealing, reaches a peak of 0.419% after 60 h followed by annealing, then decreases to 0.214% after 80 h followed by annealing, and stabilizes at 0.187% after 100 h. This suggests that the annealing temperature of 923.15 K is insufficient to induce significant grain growth. Sub-optimal temperatures limit grain growth due to insufficient thermal energy to promote their development [55]. Other studies have demonstrated that higher temperatures are required for visible grain growth and microstructural evolution. For instance, in an Fe-32%Ni alloy, annealing at 973K (approximately 973,15K) was necessary for continuous recrystallization and grain growth [55]. While the annealing temperature of 923.15 K is not optimal for grain growth, it still facilitates a certain degree of relaxation and structural stabilization. This corresponds to the observed reduction in microstrain and the formation of a stable crystalline structure in the Fe-Ni alloy [56].

4. Conclusions

This study investigated the effects of mechanical milling followed by annealing at 923.15 K on the microstructural evolution, microstrain, and crystallite size of Fe-Ni alloys. The results revealed significant transformations influenced by the milling duration and the annealing treatment. During milling, the formation of FCC γ-Ni(Fe) and BCC α-FeNi phases was observed, accompanied by structural distortions and a reduction in crystallite size favored by accumulated dislocations and internal stresses. The annealing process at 923.15 K facilitated partial relaxation of these stresses and promoted structural stabilization, as evidenced by the refinement of crystallite size, the reduction in microstrain, and the transformation of α-Fe(Ni) to γ-Ni(Fe). However, the annealing temperature of 923.15 K, while effective for structural relaxation, was insufficient for significant grain growth, particularly for samples subjected to prolonged milling. The microstrain exhibited complex behavior, indicating that higher annealing temperatures might be necessary to fully eliminate defects and to achieve optimal grain growth. These findings contribute to understanding the thermal and mechanical behavior of Fe-Ni alloys and provide insights into optimizing processing parameters to enhance their microstructural properties.

Author Contributions: Conceptualization, M.A. and M.K.; methodology, A.W. and S.A.; formal analysis, W.B.M. and S.A.; investigation, W.B.M.; writing—original draft preparation, J.-J.S. and A.W.; writing—review and editing, M.A. and J.-J.S.; supervision, J.-J.S. and M.K. All authors have read and agreed to the published version of the manuscript.

Funding: This research was funded by University of Girona, project2024-10.

Data Availability Statement: The data presented in this study are available on request from the corresponding author due to large data sets.

Conflicts of Interest: The authors declare no conflict of interest.

References

1. Guittoum, A.; Lamrani, S.; Bourzami, A.; Hemmous, M.; Souami, N.; Weber, W. Elaboration, structure, microstructure and magnetic properties of soft $Fe_{80}Ni_{20}$ nanomaterials elaborated by high energy ball milling. *Eur. Phys. J. Appl. Phys.* **2014**, *65*, 30401. [CrossRef]
2. Dalven, R. Ferromagnetic Materials. In *Introduction to Applied Solid State Physics*; Springer: Boston, MA, USA, 1990. [CrossRef]
3. Talaat, A.; Egbu, J.; Phatak, C.; Byerly, K.; McHenry, M.E.; Ohodnicki, P.R. Nanostructure refinement and phase formation of flash annealed FeNi-based soft magnetic alloys. *Mater. Res. Bull.* **2022**, *152*, 111839. [CrossRef]
4. Campos-Hernández, A.J.; Palmero, E.M.; Bollero, A. Discerning the magnetization reversal mechanism and magnetic interactions in arrays of FeNi nanowires. *J. Alloys Compd.* **2024**, *1004*, 175817. [CrossRef]
5. Gandia, D.; Gandarias, L.; Marcano, L.; Orue, I.; Gil-Cartón, D.; Alonso, J.; Arribas, A.G.; Muela, A.; Fdez-Gubieda, M. Elucidating the role of shape anisotropy in faceted magnetic nanoparticles using biogenic magnetosomes as a model. *Nanoscale* **2020**, *12*, 16081–16090. [CrossRef]
6. Ohodnicki, P.; Kautz, E.; Devaraj, A.; Yu, Y.; Aronhime, N.; Krimer, Y.; McHenry, M.; Leary, A. Nanostructure and compositional segregation of soft magnetic FeNi-based nanocomposites with multiple nanocrystalline phases. *J. Mater. Res.* **2021**, *36*, 105–113. [CrossRef]
7. Herzer, G. Grain size dependence of coercivity and permeability in nanocrystalline ferromagnets. *IEEE Trans. Magn.* **1990**, *26*, 1397. [CrossRef]
8. Khadzhay, G.Y.; Vovk, S.R.; Vovk, R.V.; Gevorkyan, E.S.; Zubenko, N.S.; Kislitsa, M.V.; Chishkala, B.O.; Feher, A.; Kollar, P.; Fuzer, J. Electrical and thermal conductivity of FeNi at low temperatures. *Low Temp. Phys.* **2020**, *46*, 939–943. [CrossRef]
9. Qin, X.Y.; Zhang, W.; Zhang, L.D.; Jiang, L.D.; Liu, X.J.; Jin, D. Low-temperature resistance and its temperature dependence in nanostructured silver. *Phys. Rev.* **1997**, *B56*, 10596. [CrossRef]
10. Weertman, J.R.; Niedzielka, M.; Youngdahl, C. *Mechanical Properties and Deformation Behavior of Materials Having Ultra-Fine Microstructures*; Nastasi, M., Parkin, D.M., Gleiter, H., Eds.; Kluwer Academic Publishers: Dordrecht, The Netherlands, 1993; p. 241.
11. Glezer, A.M.; Tomchuk, A.A.; Betekhtin, V.I.; Dunsue, B. Evolution of the structure and mechanical properties of a FeNi alloy during annealing after megaplastic deformation. *Tech. Phys. Lett.* **2017**, *43*, 399–401. [CrossRef]
12. Hong, L.B.; Fultz, B. Two-phase coexistence in Fe–Ni alloys synthesized by ball milling. *J. Appl. Phys.* **1996**, *79*, 3946–3955. [CrossRef]
13. Gheisari Kh Javadpour, S.; Oh, J.T.; Ghaffari, M. The effect of milling speed on the structural properties of mechanically alloyed Fe–45%Ni powders. *J. Alloys Compd.* **2009**, *472*, 416–420. [CrossRef]
14. Kuhrt, C.; Schultz, L. Formation and magnetic properties of nanocrystalline mechanically alloyed Fe-Co and Fe-Ni. *J. Appl. Phys.* **1993**, *73*, 6588–6590. [CrossRef]
15. Le Caër, G.; Delcroix, P.; Bégin-Colin, S.; Ziller, T. High—Energy ball-milling of alloys and compounds. *Hyperfine Interact.* **2002**, *141*, 63–72. [CrossRef]
16. Baldokhin, Y.V.; Tcherdyntsev, V.V.; Kaloshkin, S.D.; Kochetov, G.A.; Pustov, Y.A. Transformations and fine magnetic structure of mechanically alloyed Fe–Ni alloys. *J. Magn. Magn. Mater.* **1999**, *203*, 313. [CrossRef]
17. Kroon, R. Nanoscience and the Scherrer equation versus the 'Scherrer–Gottingen equation'. *S. Afr. J. Sci.* **2013**, *109*, 2. [CrossRef]
18. Kuhrt, C.; Schultz, L. Phase formation and martensitic transformation in mechanically alloyed nanocrystalline Fe—Ni. *J. Appl. Phys.* **1993**, *73*, 1975. [CrossRef]
19. Pop, V.; Isnard, O.; Chicinaş, I. Crystallographic and magnetic study of the nanocrystalline Ni_3Fe intermetallic compound formation by mechanical alloying and annealing. *J. Alloys Compd.* **2003**, *361*, 144–152. [CrossRef]
20. Arganda-Carreras, I.; Kaynig, V.; Rueden, C.; Eliceiri, K.W.; Schindelin, J.; Cardona, A.; Seung, H.S. Trainable Weka Segmentation: A machine learning tool for microscopy pixel classification. *Bioinformatics* **2017**, *33*, 2424–2426. [CrossRef]
21. Bakas, G.; Dimitriadis, S.; Deligiannis, S.; Gargalis, L.; Skaltsas, I.; Bei, K.; Karaxi, E.; Koumoulos, E.P. A Tool for Rapid Analysis Using Image Processing and Artificial Intelligence: Automated Interoperable Characterization Data of Metal Powder for Additive Manufacturing with SEM Case. *Metals* **2022**, *12*, 1816. [CrossRef]
22. Khitouni, M.; Kolsi, A.W.; Njah, N. Crystallite refinement of NiAl powders during mechanical milling. *Ann. Chim. Sci. Mat.* **2003**, *28*, 17–29. [CrossRef]
23. Degen, T.; Sadki, M.; Bron, E.; König, U.; Nénert, G. The HighScore suite. *Powder Diffr.* **2014**, *29*, S13–S18. [CrossRef]

24. Sekri, A.; Mhadhbi, M.; Escoda, L.; Suñol, J.J.; Khitouni, M.; Makhlouf, T. Synthesis and structural characterization of nanocrystalline Fe-Ni-Zr-B alloy prepared by powder metallurgy. *J. Tunis. Chem. Soc.* **2015**, *17*, 49–56.
25. Kaloshkin, S.D.; Tcherdyntsev, V.V.; Tomilin, I.A.; Baldokhin, Y.V.; Shelekhov, E.V. Phase transformations in Fe–Ni system at mechanical alloying and consequent annealing of elemental powder mixtures. *Phys. B Condens. Matter* **2001**, *299*, 236–241. [CrossRef]
26. Djekoun, A.; Boudinar, N.; Chebli, A.; Otmani, A.; Benabdeslem, M.; Bouzabata, B.; Greneche, J.M. Structure and magnetic properties of Fe-rich nanostructured Fe100-XNiX powders obtained by mechanical alloying. *Phys. Procedia* **2009**, *2*, 693–700. [CrossRef]
27. Cherdyntsev, V.V.; Pustov, L.Y.; Kaloshkin, S.D.; Tomilin, I.A.; Shelekhov, E.V.; Laptev, A.I.; Baldokhin, Y.V.; Estrin, E.I. Phase transformations during deformation of Fe-Ni and Fe-Mn alloys produced by mechanical alloying. *Phys. Met. Metallogr.* **2007**, *104*, 408–414. [CrossRef]
28. Yang, C.W.; Williams, D.B.; Goldstein, J.I. A revision of the Fe-Ni phase diagram at low temperatures (<400 °C). *J. Phase Equilibria* **1996**, *17*, 522–531.
29. Cacciamani, G.; De Keyzer, J.; Ferro, R.; Klotz, U.E.; Lacaze, J.; Wollants, P. Critical evaluation of the Fe-Ni, Fe-Ti and Fe-Ni-Ti alloy systems. *Intermetallics* **2006**, *14*, 1312. [CrossRef]
30. Cacciamani, G.; Dinsdale, A.; Palumbo, M.; Pasturel, A. The Fe-Ni system: Thermodynamic modelling assisted by atomistic calculations. *Intermetallics* **2010**, *8*, 1148–1162. [CrossRef]
31. Guittoum, A.; Layadi, A.; Bourzami, A.; Tafat, H.; Souami, N.; Boutarfaia, S.; Lacour, D. X-ray diffraction, microstructure, Mössbauer and magnetization studies of nanostructured $Fe_{50}Ni_{50}$ alloy prepared by mechanical alloying. *J. Magn. Magn. Mater.* **2008**, *320*, 1385–1392. [CrossRef]
32. Zwell, L.; Carnahan, D.E.; Speich, G.R. Lattice parameter of ferritic and martensitic Fe–Ni alloys. *Met. Trans.* **1970**, *1*, 1007–1009. [CrossRef]
33. Burgers, W. Lattice Distortion in Nickel-Iron. *Nature* **1935**, *135*, 1037–1038. [CrossRef]
34. Khitouni, N.; Mbarek, W.B.; Guittoum, A.; Suñol, J.J.; Khitouni, M.; Azabou, M. X-Ray Diffraction and Mössbauer Studies of Nanostructured $Ni_{40}Fe_{60}$ Powder: Structure Defects and Hyperfine Structure. *J. Supercond. Nov. Magn.* **2022**, *35*, 3439–3446. [CrossRef]
35. Daly, R.; Khitouni, N.; Escoda, M.L.; Isern, N.L.; Juan Jose, S.M.; Greneche, J.M.; Khitouni, M. Microstructure, Magnetic and Mössbauer Studies of Mechanically Alloyed FeCoNi Nanocrystalline Powders. *Arab. J. Sci. Eng.* **2021**, *46*, 5633–5643. [CrossRef]
36. Djekoun, A.; Otmani, A.; Bouzabata, B.; Bechiri, L.; Randrianantoandro, N.; Greneche, J.M. Synthesis and characterization of high-energy ball milled nanostructured $Fe_{50}Ni_{50}$. *Catal. Today* **2006**, *113*, 235–239. [CrossRef]
37. Ferro, A.; Montalenti, G. On the effect of the crystalline structure on the form of fatigue curves: The case of iron–nickel alloys. *Philos. Mag.* **1964**, *10*, 1043–1052. [CrossRef]
38. Mhadhbi, M.; Khitouni, M.; Escoda, L.; Suñol, J.J.; Dammak, M. Characterization of Mechanically Alloyed Nanocrystalline Fe(Al): Crystallite Size and Dislocation Density. *J. Nanomater.* **2010**, *2010*, 712407. [CrossRef]
39. Noyan, I.C.; Cohen, J.B. Determination of Strain and Stress Fields by Diffraction Methods. In *Residual Stress: Measurement by Diffraction and Interpretation*; Noyan, I.C., Cohen, J.B., Eds.; Springer: New York, NY, USA, 1987; pp. 117–163.
40. Schaffer, G.B.; McCormick, P.G. The direct synthesis of metals and alloys by mechanical alloying. *Mater. Sci. Forum* **1992**, *88–90*, 779–786. [CrossRef]
41. Ibn Gharsallah, H.; Azabou, M.; Escoda, L.; Suñol, J.J.; López, I.; Llorca-Isern, N. The magnetic and structural properties of (Fe75Al25)100−xBx alloys prepared by mechanical alloying. *J. Alloys Compd.* **2017**, *729*, 776–786. [CrossRef]
42. CNoyan, J.B. *Cohen, Residual Stress Measurement by Diffraction an Interpretation*; Springer: New York, NY, USA, 1987.
43. Révész, Á.; Ungár, T.; Borbély, A.; Lendvai, J. Dislocations and grain size in ball-milled iron powder. *Nanostruct. Mater.* **1996**, *7*, 779–788. [CrossRef]
44. Kolupaeva, S.; Semenov, M. The stored energy of plastic deformation in crystals of face-centered cubic metals. *IOP Conf. Ser. Mater. Sci. Eng.* **2015**, *71*, 012077. [CrossRef]
45. Borodin, I.N.; Petrov, Y.V. Relaxation model of dynamic plastic deformation of materials. *Mech. Solids* **2014**, *49*, 635–642. [CrossRef]
46. Baczmanski, A.; Wierzbanowski, K.; Benmarouane, A.; Lodini, A.; Lipiński, P.; Bacroix, B. Stored Energy and Recrystallization Process. *Mater. Sci. Forum* **2007**, *539–543*, 3335–3340. [CrossRef]
47. Popa, F.; Isnard, O.; Chicinaş, I.; Pop, V. Thermal evolution of the Ni_3Fe compound obtained by mechanical alloying as probed by differential scanning calorimetry. *J. Alloys Compd.* **2013**, *554*, 39–44. [CrossRef]
48. Wederni, A.; Ipatov, M.; Pineda, E.; Suñol, J.J.; Escoda, L.; González, J.M.; Alleg, S.; Khitouni, M.; Żuberek, R.; Chumak, O.; et al. Magnetic properties, martensitic and magnetostructural transformations of ferromagnetic Ni–Mn–Sn–Cu shape memory alloys. *Appl. Phys. A* **2020**, *126*, 320. [CrossRef]
49. Christien, F.; Telling, M.T.F.; Knight, K.S.; Le Gall, R. A method for the monitoring of metal recrystallization based on the in-situ measurement of the elastic energy release using neutron diffraction. *Rev. Sci. Instrum.* **2015**, *86*, 053901. [CrossRef] [PubMed]

50. Milinčić, R.; Spasojević, M.; Spasojević, M.; Maričić, A.; Randjić, S. Amorphous-crystalline Ni-Fe powder mixture: Hydrogenation and annealing effects on microstructure and electrical and magnetic properties. *Sci. Sinter.* **2016**, *48*, 343–351. [CrossRef]
51. Chang, W.-S.; Wei, Y.; Guo, J.-M.; He, F.-J. Thermal Stability of Ni-Fe Alloy Foils Continuously Electrodeposited in a Fluorborate Bath. *Open J. Met.* **2012**, *2*, 18–23. [CrossRef]
52. Ji, M.; Davis, C.; Strangwood, M. Effect of Grain Size Distribution on Recrystallisation Kinetics in an Fe-30Ni Model Alloy. *Metals* **2019**, *9*, 369. [CrossRef]
53. Madhavan, R.; Gurao, N.P.; Suwas, S. Texture evolution during annealing of large-strain deformed nanocrystalline nickel. *Philos. Mag. Lett.* **2014**, *94*, 141–149. [CrossRef]
54. Kaloshkin, S.D.; Tcherdyntsev, V.V.; Baldokhin, Y.V.; Tomilin, I.A.; Shelekhov, E.V. Mechanically alloyed low-nickel austenite Fe–Ni phase: Evidence of single-phase paramagnetic state. *J. Non-Cryst. Solids* **2001**, *287*, 329–333. [CrossRef]
55. Hodgson, P.; Cizek, P.; Beladi, H.; Taylor, A.S. Microstructure Evolution and Softening Processes Occurring during Annealing of Hot Deformed Ni-30Fe Austenite. *Mater. Sci. Forum* **2012**, *706–709*, 2134–2139. [CrossRef]
56. Liu, B.X.; Han, B.J. The Microstructure Evolution during Annealing in Large Strain Deformed Fe-32%Ni Alloy. *Mater. Sci. Forum* **2011**, *675–677*, 719–722.